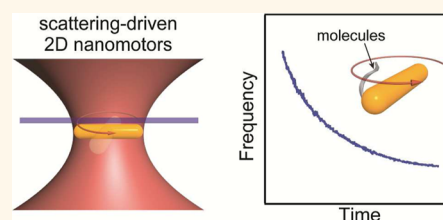


# Gold Nanorod Rotary Motors Driven by Resonant Light Scattering

Lei Shao,<sup>\*,†</sup> Zhong-Jian Yang,<sup>†</sup> Daniel Andrén,<sup>†</sup> Peter Johansson,<sup>†,\*</sup> and Mikael Käll<sup>\*,†</sup>

<sup>†</sup>Department of Applied Physics, Chalmers University of Technology, S-412 96 Göteborg, Sweden and <sup>\*</sup>School of Science and Technology, Örebro University, S-701 82 Örebro, Sweden

**ABSTRACT** Efficient and robust artificial nanomotors could provide a variety of exciting possibilities for applications in physics, biology and chemistry, including nanoelectromechanical systems, biochemical sensing, and drug delivery. However, the application of current man-made nanomotors is limited by their sophisticated fabrication techniques, low mechanical output power and severe environmental requirements, making their performance far below that of natural biomotors. Here we show that single-crystal gold nanorods can be rotated extremely fast in aqueous solutions through optical torques dominated by plasmonic resonant scattering of circularly polarized laser light with power as low as a few mW. The nanorods are trapped in 2D against a glass surface, and their rotational dynamics is highly dependent on their surface plasmon resonance properties. They can be kept continuously rotating for hours with limited photothermal side effects and they can be applied for detection of molecular binding with high sensitivity. Because of their biocompatibility, mechanical and thermal stability, and record rotation speeds reaching up to 42 kHz (2.5 million revolutions per minute), these rotary nanomotors could advance technologies to meet a wide range of future nanomechanical and biomedical needs in fields such as nanorobotics, nanosurgery, DNA manipulation and nano/microfluidic flow control.



**KEYWORDS:** nanomotors · gold nanorods · light scattering · surface plasmon · optical tweezers

Rotary nanomotors that can convert chemical, thermal, or electromagnetic energy into nanoscale mechanical motion could be of great use in various applications,<sup>1–3</sup> ranging from nanoelectromechanical systems<sup>4</sup> and nanorobotics<sup>5</sup> to DNA manipulation<sup>6</sup> and nano/microfluidic flow control.<sup>7</sup> Inspired by natural biomotors, such as ATP-driven carrier proteins, researchers have explored and developed a wide variety of rotary nanomotors driven by energy supplied by magnetic fields,<sup>8</sup> electric fields,<sup>9,10</sup> ultrasound,<sup>11,12</sup> biochemical fuels,<sup>13</sup> and optical fields.<sup>14</sup> However, the development and application of artificial rotary nanomotors are currently challenged by their costly and time-consuming fabrication steps, low mechanical output power, poor movement control, and severe environmental requirements.<sup>15</sup>

Light can exert a force on matter by means of momentum exchange through both absorption and scattering,<sup>16,17</sup> enabling fast and precise movement control of small objects. The light–matter interaction can be significantly enhanced in noble metal nanostructures that support localized surface plasmon resonances (LSPRs), enabling these structures

to overcome thermal fluctuations in an optical trap and be manipulated using wireless and contactless laser tweezers.<sup>18,19</sup> For example, individual gold nanorods with diameters smaller than ~45 nm and lengths smaller than ~100 nm have been optically trapped and aligned in three dimensions (3D) by laser beams focused by high numerical aperture objectives.<sup>20,21</sup> The magnitudes of the optical forces and torques are strongly dependent on the LSPR properties of the plasmonic structures.<sup>22,23</sup> In particular, optical torques on single metal nanocrystals have been estimated to be as large as hundreds of pN·nm,<sup>24</sup> sufficient enough to propel nanomachines and to address single-molecule processes in biological matter. Additionally, the large localized electromagnetic field enhancements brought about by LSPRs make plasmonic nanostructures efficient optical transducers of various surface processes, as demonstrated by their application in single-molecule detection and spectroscopy.<sup>25–27</sup> Optically propelled plasmonic nanostructures therefore constitute a highly interesting platform for advanced biomechanical engineering and sensing applications.

\* Address correspondence to lei.shao@chalmers.se, mikael.kall@chalmers.se.

Received for review October 7, 2015 and accepted November 13, 2015.

Published online November 13, 2015 10.1021/acsnano.5b06311

© 2015 American Chemical Society

Previous work on micron-sized plasmonic nanowires<sup>22,28,29</sup> and dielectric microdisks decorated with plasmonic structures<sup>14</sup> showed sustained optical rotation in solution, but only at very low spinning frequencies of the order of a few Hz. A recent study of  $\sim 400$  nm diameter gold colloids utilized the optical torque induced by absorption of circularly polarized photons to spin the particles at rotation frequencies up to  $\sim 3$  kHz, but at the expense of substantial laser heating.<sup>30</sup> The generation of optical torques through light scattering, though challenging for subwavelength structures, could potentially allow greater freedom of operation than torque from absorption<sup>23</sup> and also prevent the nanostructures from being severely heated. In this study, we choose to work with gold nanorod motors with lengths of the order of 130–190 nm and diameters of  $\sim 65$ –85 nm because their reduced symmetry and comparatively large size, though still in the deep subwavelength regime, boost transfer of angular momentum due to light scattering, which means that absorption and laser heating can be significantly reduced. Moreover, chemically synthesized gold nanorods exhibit excellent crystalline quality and their LSPRs can be easily tuned from the visible to the near-infrared by varying their length-to-width aspect ratio.<sup>31,32</sup> However, the radiation pressure associated with the large scattering cross-section makes it

challenging to achieve stable optical trapping in 3D. We therefore trapped the gold nanorods in 2D against a glass substrate. We achieved extremely fast rotation of the nanorods in aqueous solution, with spinning frequencies reaching up to 42 kHz (2.5 million revolutions per minute) at low laser powers. We demonstrate that the optical torques driving the nanorods, which are induced by transfer of angular momentum from circularly polarized photons, are greatly amplified by plasmon enhanced scattering and therefore highly dependent on the nanorod LSPR properties. The nanorod motors could be kept rotating at constant speeds for hours with very limited photothermal heating, which made it possible to use the rotation frequency as a probe of molecular binding with high sensitivity.

## RESULTS AND DISCUSSION

**Rotation of Gold Nanorods in an Optical Trap.** The nanorods were prepared by a seed-mediated growth method<sup>33</sup> (Supporting Information Method S1, Figure S1) and they were trapped in 2D against a standard cover glass in an optical tweezers setup by an 830 nm circularly polarized laser beam (Figure 1a and b). We first used gold nanorods with an average length/diameter of 164/84 nm (Figure 1c) and a longitudinal LSPR at 762 nm. The 830 nm laser-line is on the low-frequency flank of the nanorod LSPR and therefore provides

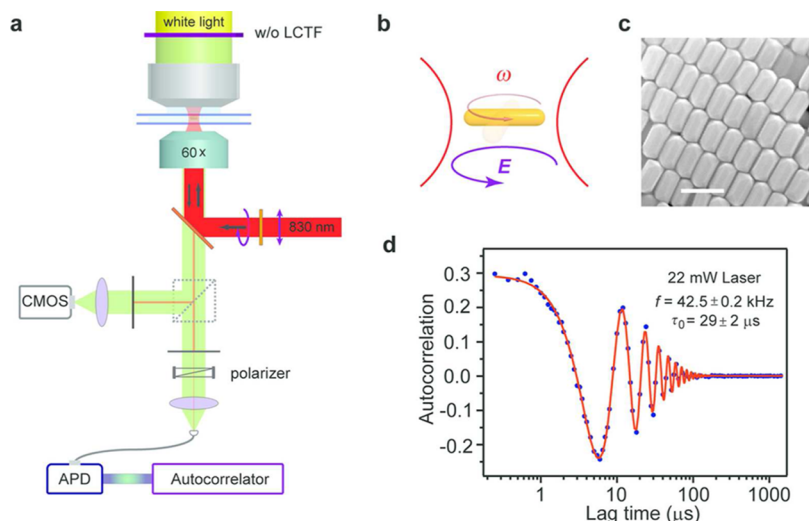


**Figure 1.** Ultrafast spinning of gold nanorods in water with frequencies of up to 42 kHz. (a) Schematic of the setup for optical trapping, rotation frequency measurement, and spectrum acquisition. A single gold nanorod (zoomed views shown in (b)) is trapped by a circularly polarized near-infrared laser beam ( $\lambda = 830$  nm), which provides angular momentum that forces the nanorod to rotate. The nanorod is trapped in 2D against a cover glass by the radiation pressure and the optical gradient force. The sample is also illuminated with white light through a dark field condenser. The light scattered from the nanorod is recorded by a CMOS camera or an avalanche photodiode (APD) connected to an autocorrelator. We use the same optical setup for dark-field scattering spectroscopy by adding a liquid crystal tunable filter (LCTF) to the optical path (Supporting Information Figure S5). (c) Scanning electron microscope image of the gold nanorods with an average length and diameter of 164 and 84 nm, respectively, and with a longitudinal localized surface plasmon resonance (LSPR) wavelength at 762 nm in solution. Scale bar, 200 nm. (d) Intensity autocorrelation plot for a nanorod shown in c subject to 22 mW circularly polarized laser light. The solid line represents a fit to the data using the theoretically derived correlation function. The autocorrelation oscillation corresponds to a rotation frequency  $f$  of 42.5 kHz and an autocorrelation decay time  $\tau_0$  of 29  $\mu$ s. The  $f$  and  $\tau_0$  values were derived by fitting the scattering autocorrelation function to the measured intensity autocorrelation data. The  $f$  and  $\tau_0$  uncertainties corresponding to 95% confidence intervals were calculated from the fit, which has a coefficient of determination ( $R^2$ ) of 0.9969.

an attractive and highly enhanced optical gradient force.<sup>19</sup> The rotational dynamics was monitored by an ultrafast CMOS camera or by recording the intensity autocorrelation function  $C(\tau) = \langle I(\tau)I(0) \rangle$ , where  $\tau$  is the lag-time, of the nanorods elastic light scattering (Figure 1 and Supporting Information Method S2).<sup>30</sup> The correlator setup is easy to combine with dark-field spectroscopy measurements and we can measure the rotational dynamics up to very high spinning frequencies. We observed a fast periodic oscillating scattering autocorrelation function (Figure 1d), similar to that reported in ref 30. The periodic behavior is caused by the nanorod rotation and it disappears if we switch to linear laser polarization (Supporting Information Figure S2). The scattering intensity variations recorded by the fast CMOS camera and the autocorrelator agree well with each other (Supporting Information Figure S3). The CMOS camera also recorded the trace of the optical center of mass for the rotating nanorod (Supporting Information Figure S3). Although we did not observe a clear effect of structural/hydrodynamic asymmetries on the translational Brownian motion of the trapped nanocrystals,<sup>24</sup> more experimental studies are required to disclose the precise dynamics of the translational motion of the rotating nanorods, as well as possible coupling between translational and rotational degrees of freedom. Further analysis revealed that the optically trapped nanorods were rotating about their short axes in a plane normal to the optical axis (Supporting Information Method S3, Figure S4), which is consistent with previously published results of nanorods trapped by linearly polarized light.<sup>20,21</sup> At a laser power of 22 mW, the autocorrelation oscillation for one of the trapped nanorods reached as high as 85 kHz, corresponding to a 42.5 kHz (2 550 000 rpm) rotation frequency. To the best of our knowledge, this is the fastest rotation of any man-made or natural motor in aqueous solution recorded to date.<sup>12,30</sup>

**Torque and Rotational Dynamics Calculations.** A spherically symmetric particle illuminated by circularly polarized light experiences a torque due to absorption of light, but scattering does not contribute to the torque because any scattered photon has the same angular momentum after the scattering event as before. This is no longer true for asymmetric particles in which case the angular momentum state of a photon may change upon scattering. In a first approximation, the generation of scattering torque can be analyzed by considering an elongated particle illuminated by a plane wave in the dipole limit. Let  $\alpha_{0x}$  and  $\alpha_{0y}$  be the electric dipole polarizabilities along the major and minor axes in a plane perpendicular to the propagation direction of the incident light. Radiation reaction modifies the full polarizabilities to become

$$\alpha_x = \frac{\alpha_{0x}}{1 - ik^3 \sqrt{\epsilon} \alpha_{0x} / (6\pi\epsilon_0)} \quad (1)$$

with a similar expression for  $\alpha_y$ . Here  $k = \omega_0/c$  and  $\epsilon$  is the dielectric constant of the surrounding medium. The time-averaged torque acting on the particle along the propagation direction can in this case be calculated as<sup>34</sup>

$$M_{\text{opt}} = \frac{1}{2} \text{Re}[\vec{p}^* \times (\vec{\alpha}_0^{-1} \vec{p})] \quad (2)$$

where  $\vec{p}$  is the particle dipole moment. For a circularly polarized incident field  $\vec{E} = (\hat{x} + i\hat{y})E_0/\sqrt{2}$ , and keeping terms up to order  $k^3$  assuming weak scattering, the torque can be written

$$M_{\text{opt}} \approx \frac{E_0^2}{4} \left\{ \text{Im}[\alpha_{0x} + \alpha_{0y}] + \frac{k^3 \sqrt{\epsilon}}{6\pi\epsilon_0} \text{Re}[(\alpha_{0x} - \alpha_{0y}^*)\alpha_{0x} + (\alpha_{0y} - \alpha_{0x}^*)\alpha_{0y}] \right\} \quad (3)$$

Here the first term represents the torque due to light absorption by the particle, while scattering contributions enter the second term. Specifically for an asymmetric but nonabsorbing particle for which  $\alpha_{0x}$  and  $\alpha_{0y}$  are real, the absorption contribution vanishes, and the scattering contribution can be written

$$M_{\text{opt}} \approx \frac{E_0^2 k^3 \sqrt{\epsilon}}{24\pi\epsilon_0} (\alpha_{0x} - \alpha_{0y})^2 \quad (4)$$

According to eqs 3 and 4, it is clear that asymmetry is required to have any scattering torque for small plasmonic nanoparticles.

The periodic autocorrelation oscillation in Figure 1d decays exponentially due to rotational Brownian motion and this result can be understood by solving the equation of motion for the rod:<sup>30</sup>  $J(d\omega/dt) = M_{\text{opt}} + M_f + M_s$ , where  $J$  is the moment of inertia of the nanorod,  $\omega$  is the instantaneous angular velocity of rotation,  $M_f$  is a friction torque, and  $M_s$  is a stochastic torque. The optical torque arising from absorption can be evaluated as<sup>35</sup>  $M_{\text{abs}} = \sigma_{\text{abs}} \cdot I_{\text{inc}}/\omega_0$  for a light intensity  $I_{\text{inc}}$ , photon energy  $\hbar\omega_0$ , and particle absorption cross section  $\sigma_{\text{abs}}$ , which can be obtained from finite-difference time-domain (FDTD) simulations. The optical torque caused by scattering cannot be expressed by an equally simple equation. Instead, we calculated the total optical torque  $M_{\text{opt}}$  acting on the gold nanorods using the Maxwell Stress Tensor (MST) method, with the field data from FDTD simulations.<sup>18,23</sup> As shown in Supporting Information Figure S6, the generated torque  $M_{\text{opt}}$  forces the nanorod to rotate in the same direction as that of the  $E$  field of the incident light. The scattering contribution to the torque can be calculated as  $M_{\text{sca}} = M_{\text{opt}} - M_{\text{abs}}$ . We can thus distinguish the contributions from scattering and absorption accordingly. To calculate  $M_f$ , a nanorod with length  $L$  and diameter  $D$  is modeled by an elongated prolate spheroid with semimajor axis  $L/2$  and semiminor axis  $D/2$ . For laminar flow (low Reynolds number), the viscous friction torque  $M_f$  from the surrounding liquid

can be expressed as<sup>36</sup>  $M_f = -\pi\eta L^3\omega\gamma$ , where  $\eta = \eta(T)$  is the temperature-dependent dynamical viscosity of the surrounding liquid<sup>30,37</sup> and  $\gamma$  is a geometrical factor that only depends on the spheroid eccentricity. We neglect friction contribution from the top glass surface for simplicity, which means that  $\eta$  should be regarded as an effective viscosity parameter.

At steady state, the optical driving torque  $M_{\text{opt}}$  and frictional torque  $M_f$  are balanced, which yields an average rotation frequency  $f_{\text{avg}} = M_{\text{opt}}/(2\pi^2\eta\gamma L^3)$ . The nanorod rotation is also affected by a thermal stochastic torque  $M_s$ , which increases in strength with increasing friction and temperature<sup>38,39</sup> and causes fluctuations in the angular velocity of the rod around the average  $\omega_{\text{avg}}$ . The angular velocity deviates from the average by an amount of the order of  $(k_B T/J)^{1/2}$  and the deviations from the average persist on a time scale of the order of  $J/(\pi\eta\gamma L^3)$ . Taking the distribution in angular velocity into account, we can calculate the scattering autocorrelation function to be<sup>30</sup>  $C(\tau) = I_0^2 + 0.5I_1^2 \exp(-\tau/\tau_0) \cdot \cos(4\pi f_{\text{avg}}\tau)$ , where  $I_0$  is the average intensity,  $I_1$  is the amplitude of the intensity fluctuation that occurs as a result of the particle rotation, and  $\tau_0 = \pi\eta\gamma L^3/(4k_B T)$  is the autocorrelation decay time. This allows us to extract  $f_{\text{avg}}$  and  $\tau_0$  from a fit to the experimental  $C(\tau)$ . We note in passing that the definition of temperature for a particle performing so-called “hot Brownian motion” is nontrivial and of high current interest.<sup>40,41</sup> However, since the autocorrelation oscillation is due to a rapid rotary motion, it is appropriate to use the nanorod surface temperature  $T$  for determining the viscosity of the liquid in its immediate surroundings. We used finite element simulations to calculate  $T$  (Supporting Information Figure S7), which then allow us to predict  $f_{\text{avg}}$  and  $\tau_0$  for a certain incident laser power. The values of all the parameters for the calculation of  $f_{\text{avg}}$  and  $\tau_0$  are shown in Supporting Information Table S1.

#### LSPR-Dependent Rotational Dynamics of Nanorod Motors.

The rotational dynamics of the gold nanorods strongly depend on their plasmonic responses and the laser power. We synthesized colloidal nanorods with lengths varying between  $\sim 130$  nm and  $\sim 170$  nm but with a fixed diameter of  $\sim 65$  nm to investigate this dependence (Figure 2a). The rods have extremely small polydispersity and their extinction spectra (Figure 2b) exhibit a distinct longitudinal LSPR that varies systematically with nanorod length. The light–matter interaction increases as the LSPR approaches the laser line, which leads to faster rotation and shorter autocorrelation decay times of the gold nanorods (Figure 2c and d). The photon angular momentum transfer is maximized when the LSPR coincides with the laser wavelength and a 10 mW laser power is then enough to spin a nanorod at  $\sim 42$  kHz. For the  $173 \times 65$  nm rods, we estimate the optical torque to be 37 pN·nm under resonance conditions for an incident intensity of  $1 \text{ mW} \cdot \mu\text{m}^{-2}$ ,

which provides a driving power of 700 aW. The experimentally measured values of the rotation frequencies and autocorrelation decay times are in excellent overall agreement with the calculated  $f_{\text{avg}}$  and  $\tau_0$  (Figure 2f,g). The small discrepancies are probably mainly due to uncertainties concerning the actual particle surface temperature, friction torque, and laser power input, for example caused by our neglect of cover glass heat conduction, reflection and friction, as well as errors caused by using a spheroid model to simulate the friction torque. We could not perform successful rotation experiments for nanorods with LSPR longer than 830 nm, since the laser trap provides a repulsive gradient force when the laser line is on the high-frequency flank of the nanorod LSPR.

Both the scattering and the absorption torques are maximized at the LSPR wavelength (Figure 2e), but the scattering torque can be six times larger than the absorption contribution. This is a distinct advantage compared to spherical particles, for which there is no scattering-induced torque. However, the absorption in the nanorods still results in laser heating for high laser powers and this photothermal effect can be quantified through the experimentally measured autocorrelation decay time, which only depends on temperature for a given nanorod morphology,  $\tau_0(T) = \pi\eta(T)\gamma L^3/(4k_B T)$ . The measured temperature  $T$  extracted from the autocorrelation measurements can thus be used to estimate the heating of the water in the vicinity of the trapped nanorod. We analyzed the autocorrelation signals for gold nanorods with different sizes and calculated  $T$  at varying trapping laser powers. The results show that the experimentally estimated  $T$  increases almost linearly with laser power, in excellent overall agreement with the calculated nanorod surface temperature obtained from finite element simulations (Supporting Information Figure S8, S9). However, at high laser powers, the experimentally derived temperatures are clearly lower than the values from simulations, indicating the onset of processes not accounted for in the model. We found that the measured rotation frequencies (Figure 2c) began to deviate from the theoretical predictions (Figure 2f) when the temperature excess is more than approximately 140 °C compared to room temperature (22 °C) for all the rods. Moreover, at highest powers, which correspond to a temperature excess of the order  $\sim 200$  °C, the rods get stuck on the cover glass surface and stop rotating (Figure 2c and Supporting Information Figure S8). Although there can be many causes behind these effects, including particle reshaping and changes in interfacial properties, it is interesting to note that a recent study of laser-heated gold nanoparticles, by Hou *et al.*,<sup>42</sup> indicate a phase transition to a regime characterized by nanobubble formation at around 450 K for particles of radius  $\sim 100$  nm. We did not observe any vapor bubble formation in any of our



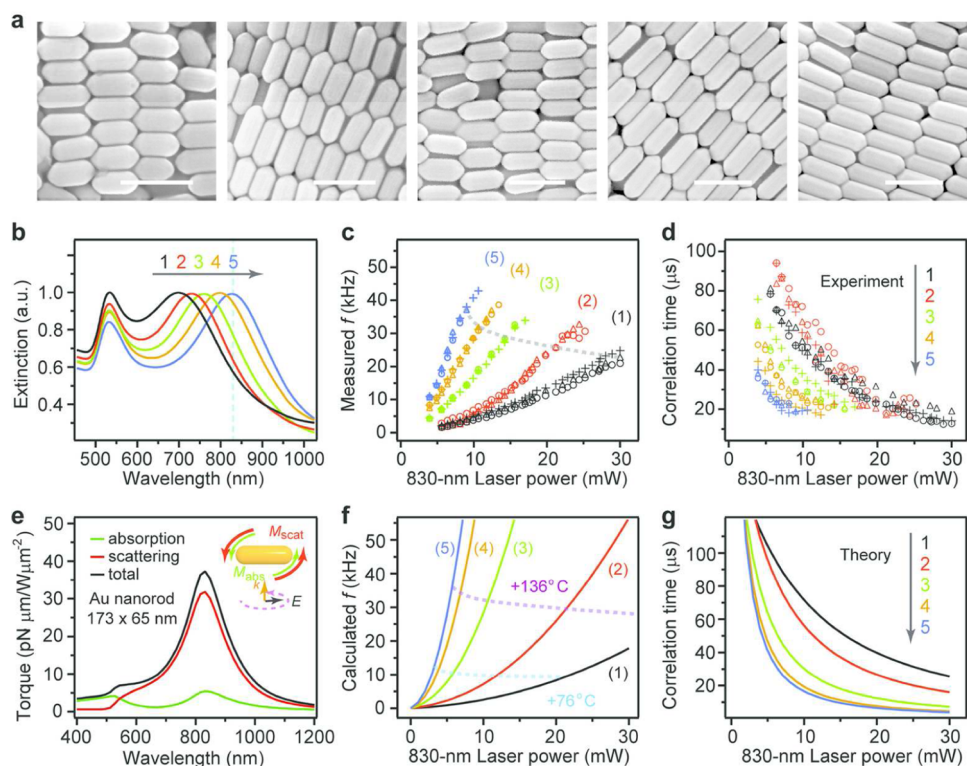


**Figure 2. Rotational dynamics versus nanorod length.** (a) SEM images of gold nanorods with different LSPR wavelengths. The average lengths/diameters of the nanorods in the figure (from left to right) are  $(134 \pm 10)/(64 \pm 5)$  nm,  $(147 \pm 10)/(65 \pm 5)$  nm,  $(157 \pm 10)/(65 \pm 5)$  nm,  $(169 \pm 10)/(66 \pm 5)$  nm, and  $(173 \pm 8)/(65 \pm 5)$  nm, respectively (scale bars = 200 nm). (b) Measured extinction spectra of the five gold nanorod samples in aqueous solutions. Two resonance peaks can be observed. The low-energy peak, which corresponds to the nanorod longitudinal LSPR, shifts from 699 to 826 nm. The high-energy peak corresponding to the transverse LSPR hardly changes. The dashed line indicates the laser wavelength (830 nm) used in the experiments. (c,d) Experimentally measured power dependences of the rotation frequencies (c) and the autocorrelation decay times (d) for the nanorods shown in a and b. The dashed line in (c) indicates the change in behavior, possibly indicating nanobubble formation, discussed in the text. (e) Calculated optical torque contributions from absorption and scattering for the  $173 \times 65$  nm gold nanorod. The scattering contribution dominates for all investigated nanorods, as indicated in the inset. (f,g) Theoretically calculated power dependences of the rotation frequencies (f) and the correlation times (g) for the nanorods. The calculated power dependence of the nanorod surface temperature for different rods is shown in Supporting Information Figure S8b. Isothermal curves therefore can be drawn in (f) by connecting the data points corresponding to the same temperature for different nanorods. The dashed lines in (f) indicate calculated isotherms, that is, points when the temperature excess compared to room temperature is constant, in this case  $\Delta T = 76$  and  $136$  °C, respectively. Direct graphical comparisons between experimentally measured and theoretically calculated rotation frequencies, correlation times, and temperature values are shown in Supporting Information Figure S9.

experiments, but this does not exclude that a nanoscopic layer of vapor form around certain regions of the particles at high enough laser intensities.

**Optimized Conditions for Nanorod Rotation.** We further compared the scattering and absorption torques for the gold nanorod shown in Figure 2e by plotting the calculated cross section ratio  $\sigma_{\text{sca}}/\sigma_{\text{abs}}$  and torque ratio  $M_{\text{sca}}/M_{\text{abs}}$  as a function of wavelength. As shown in Figure 3a, the two ratios are close to each other around the two resonance wavelengths for all the investigated nanorods. Since  $M_{\text{abs}}/\sigma_{\text{abs}} = I_{\text{inc}}/\omega_0$ , this implies that the scattering torque at the LSPR wavelengths  $\lambda_{\text{LSPR}}$  (defined as the peak wavelengths of the extinction spectra) can be approximately estimated as  $M_{\text{sca}}(\lambda_{\text{LSPR}}) \approx \sigma_{\text{sca}}(\lambda_{\text{LSPR}})I_{\text{inc}}/\omega_0$ . This can be understood from the fact that the scattered light at resonance is almost linearly polarized for the case when the two nanorod resonances are well separated and the

polarizability of the rod is strongly anisotropic (i.e.,  $|\alpha_{\text{ox}}| \gg |\alpha_{\text{oy}}|$  or  $|\alpha_{\text{ox}}| \ll |\alpha_{\text{oy}}|$ ). The angular momenta of the incident circularly polarized photons are then almost completely transferred to the nanorod.

We investigated the variation in scattering and absorption torques with nanorod size by first calculating the optical torques for rods with the same diameter  $D$  but different lengths  $L$  for a fixed laser wavelength. As expected, both the scattering and absorption torques increase when  $\lambda_{\text{LSPR}}$  redshifts toward the laser line as  $L$  increases (Figure 3b), but the scattering contribution to the total optical torque increases, from  $\sim 70\%$  to  $\sim 86\%$ , as  $\lambda_{\text{LSPR}}$  redshifts (see also Supporting Information Table S1). We also calculated the optical torques at  $\lambda_{\text{LSPR}}$  for nanorods with fixed aspect ratio  $L/D = 2$  but varying  $D$ . As the size increases (Figure 3c), the absorption torque first rapidly increases but then levels off, while the scattering torque exhibits a continuous

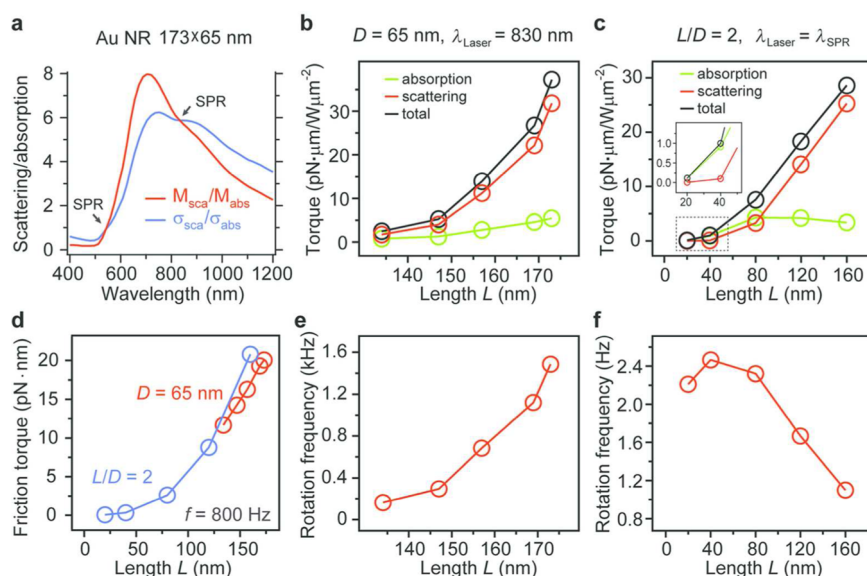


**Figure 3.** Optimized conditions for rotating gold nanorods. (a) Comparison between contributions from scattering and absorption in optical cross sections and torques for the  $173 \times 65$  nm gold nanorod shown in Figure 2e. The spectral dependence of the cross-section ratio  $\sigma_{\text{sca}}/\sigma_{\text{abs}}$  and the torque ratio  $M_{\text{sca}}/M_{\text{abs}}$  are in general not the same, but at the two resonance wavelengths they almost coincide, i.e.,  $\sigma_{\text{sca}}/\sigma_{\text{abs}} \approx M_{\text{sca}}/M_{\text{abs}}$ . (b) Calculated optical torques at 830 nm for nanorods approximating the ones shown in Figure 2a. The diameters of the nanorods  $D$  were fixed to 65 nm. Both the scattering and the absorption torques increase as the longitudinal LSPR of the nanorod approaches the laser line. (c) Calculated optical torques at the longitudinal LSPR wavelength for nanorods with different sizes. The aspect ratio of the rods was fixed at  $L/D = 2$  while the length varied from 20 to 160 nm. The inset shows a zoomed in view of the part enclosed by the dashed box. (d) Calculated friction torques as a function of  $L$  for nanorods with either a fixed aspect ratio or a fixed diameter. The calculations assume a fixed temperature (room temperature) and rotation frequency (0.8 kHz). (e, f) Calculated rotation frequency for nanorods with a fixed diameter  $D = 65$  nm ( $\lambda_{\text{laser}} = 830$  nm) and a fixed aspect ratio  $L/D = 2$  ( $\lambda_{\text{laser}} = \lambda_{\text{LSPR}}$ ), respectively, at room temperature. The laser intensity was fixed at  $1 \text{ mW}/\mu\text{m}^2$ .

increase such that its contribution to the total torque changes from 4% to 88% as  $D$  increases from 10 to 80 nm. To find optimized rotation conditions, we also calculated the friction torques for the nanorods above. For fixed temperature and rotation frequency, the friction torque scales as  $L^3$  (Figure 3d). At low incident intensities, for which laser-induced heating can be neglected, the calculations demonstrate that (1) the rotation speed increases as  $\lambda_{\text{LSPR}}$  approaches the laser wavelength for gold nanorods with similar sizes (Figure 3e); (2) for nanorods driven at resonance ( $\lambda_{\text{laser}} = \lambda_{\text{LSPR}}$ ), the equilibrium frequency first increases and then decreases as the nanorod size increases (Figure 3f). The variation in optical and friction torques *versus* size thus results in an optimized condition for maximal rotation frequency at a given laser intensity, and for the particular case of  $L/D = 2$ , the optimal diameter is in the range of 20–40 nm. However, for applications where laser heating has to be minimized, larger gold nanorods may be preferred due to their scattering dominated optical torque. It should be noted that the above considerations are based on plane wave excitation. In an actual trapping experiment, either in 2D or 3D, one also needs to take into account the variations in the optical gradient forces and radiation pressure with particle size and shape. For example, large gold nanoparticles are easy to trap in 2D because of the large in-plane gradient force but difficult to trap in 3D because of the large radiation pressure.<sup>43</sup>

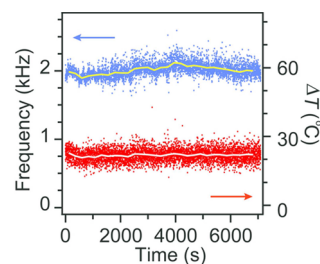


**Figure 4.** Continuous rotation of a single nanorod for 2 h. A gold nanorod ( $164 \times 84$  nm) was kept rotating in a 5 mW Laser trap (830 nm) for 2 h and the scattering autocorrelation signals were recorded every 1.3 s. The rotation frequency  $f$  (blue dots) was directly obtained from the autocorrelation data. The local temperature excess  $\Delta T$  (red dots) of the nanorod was extracted from the measured autocorrelation decay. Solid lines represent running average values integrated over 2 min.

**Durability and Stability of Gold Nanorod Motors.** The scattering induced torque enables us to rotate the nanorods fast over long time periods and with low photothermal heating. For a laser power of 5 mW, a gold nanorod ( $164 \times 84$  nm) could be rotated stably for  $>2$  h at  $2 \pm 0.2$  kHz and with a surface temperature excess of  $\sim 22 \pm 5$  °C (Figure 4). The fluctuations in measured rotation frequency and surface temperature excess are mainly attributed to uncertainties from the fitting and translational diffusion of the nanorod in the optical trap (see Supporting Information Discussion S1). The continuous

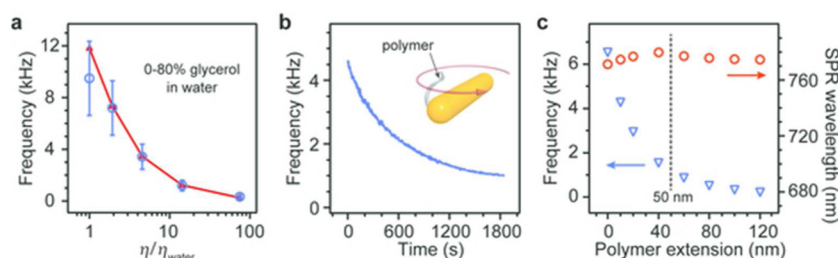


**Figure 5.** Application of spinning gold nanorods for viscosity and molecular attachment measurements. Gold nanorods with an average length/diameter of 164 nm/84 nm were trapped at low laser powers and used to probe viscosity changes and binding of a thiolated polymer in solutions. (a) Experimentally measured (blue) and calculated (red) spinning frequency versus solution viscosity relative to water. The laser power was fixed at 7 mW and 20 nanorods were examined for each mixture solution. The rotation frequencies of the nanorods were obtained by fitting the scattering autocorrelation function  $C(\tau)$  to the measured intensity autocorrelation data. We then plotted the average rotation frequency of the 20 rods measured in each mixture solution together with error bars corresponding to 95% confidence intervals. (b) Rotation frequency versus time during the adsorption of thiolated mPEG onto a spinning gold nanorod trapped using 6 mW laser power. The rotation frequency decreases from 4.5 kHz to 1.0 kHz during 30 min. (c) Calculated equilibrium spinning frequency and LSPR wavelength versus polymer extension for a polymer-encapsulated nanorod. The chain length of a fully extended polymer can be as large as 114 nm, inducing a large enough friction to slow down the nanorod rotation. The relative change observed and calculated for the rotation-based molecular sensing is much higher than for the LSPR-based sensing.

rotation in Figure 4 corresponds to  $>14\,000\,000$  cycles in total, much more than for any synthetic rotary nanomotor reported to date.<sup>10</sup>

Small gold nanorods have been reported to undergo surface melting in an optical trap.<sup>44</sup> We therefore checked the thermal stability of the nanorods by recording the scattering correlation function while sweeping the input laser power  $P$  from 5.6 mW to 17.6 mW and back again for a few particles. The  $f(P)$  and  $T(P)$  curves thus obtained (Supporting Information Figure S10) showed smooth variations and no hysteresis within experimental errors, thus, indicating that the LSPR and morphological properties of the nanorods were conserved up to laser powers corresponding to a surface temperature of the order  $T \approx 400$  K. It should be noted that at higher laser powers, which correspond to ultrahigh rotation frequencies, the rotation is not very stable, which is probably due to nanocrystal reshaping effects and surface property changes. Detailed investigations of the nanorod dynamics at high laser powers are under way and will be presented in a future article.

#### Gold Nanorod Motors for Viscosity and Molecular Sensing.

The stable rotation, reduced heat generation and chemical inertness pave the way for using the gold nanorod motors in various applications, such as biosensing,<sup>45</sup> drug release,<sup>10</sup> and construction of nanomechanical devices.<sup>9</sup> We examined their performance as transducers for probing solution viscosity changes and molecular attachment. Figure 5a shows a case where we used a 7 mW laser trap to rotate the rods in glycerol–water mixtures with varying glycerol concentrations. The rotation frequency decreased rapidly in response to the increasing viscosity and this trend could be accurately reproduced by calculations. The sensitive rotation response to surrounding viscosity indicates a new powerful route toward molecular sensing, in addition to the widely employed technique of monitoring the LSPR shift induced by localized refractive index changes.

The attachment of molecules onto the nanorod surface changes both the local refractive index and the local viscosity around the nanorod and therefore perturbs both the mechanical spinning and the optical plasmonic response accordingly. As an example, Figure 5b shows how the rotation of a nanorod can be tracked in time after it has been subject to a dilute solution of thiolated methoxy-terminated poly(ethylene glycol) (mPEG-SH, MW 20 kDa, 7.5  $\mu$ M) (Supporting Information Method S4). The rotation slowed down rapidly from 4.5 to 1.0 kHz (78%) in 30 min due to the binding of molecules. In comparison, the LSPR peak only shifts by  $\sim 5$  nm ( $\sim 0.6\%$ ) if the same type of nanorods, anchored on glass, are incubated for 2h in the same solution (Supporting Information Figure S11).

The rapid decrease of rotation frequency shown in Figure 5b may result from the following possibilities: (1) the free polymers in solution are gradually adsorbed onto the glass–water interface, leading to an increase of the viscosity near the interface; (2) the adsorption of molecules on the gold surface continuously shifts the LSPR of the rod, introducing changes in the optical torque; (3) the polymers chemically bind to the gold surface, providing an extra drag force that slows down the nanorod rotation. Because of the low polymer concentration, we can neglect the viscosity increase near the glass–water interface brought by molecular adsorption<sup>46</sup> and the solution viscosity is almost the same as that of water. In order to investigate the polymer binding effects, we modeled the polymer layer as a dielectric shell surrounding the rod for a simple approximation (see Methods). The shell thickness represents the length of the stretchable polymer with one end anchored on the gold nanorod surface. As the shell thickness increases, the calculated LSPR red shifts by at most 8 nm (Figure 5c), which agrees well with the LSPR measurements. This LSPR shift produces a maximum of 10% increase in the optical torque at 830 nm.

However, the change in optical torque is overwhelmed by the simultaneously increased friction torque, which makes the rotation speed drop significantly (Figure 5c). Our calculations can thus well explain the experimental observations and also suggest that the effective thickness of the polymer is  $\sim 50$  nm, which is about half of the total unfolded length. Polymer chains some 50 nm away from the metal surface is beyond the LSPR sensing range. This explains the significant increase in friction (Figure 5c) in spite of an insignificant LSPR shift.

## CONCLUSIONS

In summary, we have shown that circularly polarized laser light can drive ultrafast spinning of single-crystalline plasmonic gold nanorods in solution through optical torques dominated by tunable resonant light scattering. The gold nanorod motors exhibit stable and durable rotation properties and significantly reduced photothermal heating. We have demonstrated their applicability for analysis of local viscosity and molecular attachments. The latter effect, which could be especially useful for measurements of interactions and conformational changes of large biomacromolecules and polymers, provides an interesting

complement to classical LSPR refractometric sensing, which exhibits a limited spatial sensing range due to the localized LSPR fields extending only a few nanometers away from the particle surface.

We further believe that the results reported here open exciting possibilities in nanoelectromechanical system technology. Because of their considerable optical torque and driving power, rapidly rotating gold nanorods could serve as actuators for inducing fluidic motion in nanofluidic channels<sup>9</sup> and mechanical triggers of chemical reactions. Because of their nanoscale size, colloidal nature and generic biocompatibility, the application of rotating gold nanorods could probably be rather easily extended to encompass biological systems and *in vivo* situations, for example by offering a new tool for mechanically probing and manipulating living cells from the inside.<sup>11</sup> The rotational dynamics-based sensing mechanism could of course also be combined with other molecular analysis techniques developed for plasmonic structures, including LSPR refractometric sensing, surface-enhanced Raman scattering, and plasmon-enhanced fluorescence spectroscopy, thereby transforming the rotating nanorods into truly generic optomechanical sensor elements.

## METHODS

**Sample Preparation.** Gold nanorods were prepared by a wet-chemical method involving seed-mediated growth and anisotropic oxidation (see Supporting Information Method S1).<sup>32,33</sup> The particle morphologies were determined by scanning electron microscopy (Leo Ultra 55 FEG SEM, Carl Zeiss AB). Droplets of diluted colloidal nanorod suspensions were placed between two glass slides separated by a 100  $\mu\text{m}$  spacer for the optical trapping experiments.

Molecular sensing experiments were carried out in 7.5  $\mu\text{M}$  solutions of methoxy-terminated poly(ethylene glycol) thiol ( $\text{CH}_3\text{O}-(\text{CH}_2\text{CH}_2\text{O})_N-\text{CH}_2\text{CH}_2-\text{SH}$ , mPEG-SH,  $N \approx 455$ , MW 20 kDa), using the  $164 \times 84$  nm gold nanorods. More details about the molecular sensing experiments can be found in the Supporting Information Method S4.

**Optical Experiments.** The optical tweezers setup was constructed on an inverted microscope (Nikon TE300) equipped with white-light dark-field illumination for the detection of the nanoparticles.<sup>30</sup> A near-infrared laser beam (830 nm) was focused onto the sample by an air microscope objective (Nikon 60 $\times$ , NA = 0.7). A quarter-wave plate that can be flipped in and out of the optical beam path without affecting the alignment is used to convert between linear and circular laser polarization. An oil-immersion dark-field condenser (NA = 1.2–1.43) was employed for the white light illumination. Light scattered by a spinning nanorod was passed through a linear polarizer and recorded using a fiber-coupled avalanche photo diode (APD, maximum sampling rate 100 MHz) connected to an autocorrelator (ALV-5000). The spinning frequencies could be obtained by fitting the autocorrelation signals (see Supporting Information Method S2). Each measurement by the autocorrelator has a duration of 1 s and the obtained spinning frequency represents its average in the 1 s measurement time. Single particle scattering spectra were recorded by hyper-spectral imaging using a liquid crystal tunable filter (LCTF, Varispec) and a CMOS camera (Andor Neo 5.5 sCMOS) (Supporting Information Method S3).

**Theoretical Calculations.** The absorption, scattering, and extinction cross sections of gold nanorods were obtained from finite-difference time-domain (FDTD) simulations. The field data

required for the calculation of the Maxwell Stress Tensor, which is a key parameter to calculate the time average optical torques on the nanorods, were also recorded in the FDTD simulations. The simulations were carried out with FDTD Solutions 8.7 (Lumerical, Canada). During simulations, a light pulse in the wavelength range of 400–1200 nm was launched into a box containing the target nanorods to simulate a propagating plane wave interacting with the nanorods. The gold dielectric function was represented by fitting the experimental data points from Johnson and Christy.<sup>47</sup> The refractive index of the surrounding medium was first taken to be 1.333 to simulate water for the calculation of cross sections (Supporting Information Figure S1c) and optical torques. To simulate plasmon resonance response to molecular attachments for gold nanorods, the polymer layer was modeled as a dielectric shell with its thickness  $h$  varying from 0 to 120 nm. The refractive index of the shell decreases as the polymer chain is stretched. In the simulation, the refractive index of the molecular layer was taken as 1.353 ( $h \leq 40$  nm), 1.346 ( $h = 60$  nm), 1.343 ( $h = 80$  nm), 1.341 ( $h = 100$  nm), and 1.339 ( $h = 120$  nm), respectively.<sup>48</sup>

The total optical torque  $M_{\text{opt}}$  acting on the gold nanorods was calculated using the Maxwell Stress Tensor (MST) method,<sup>18</sup> with the field data from FDTD simulations. Specifically, for a fixed nanorod exposed to a steady incident flux, the time-averaged total radiation torque can be obtained from an area integral of the time-averaged MST  $\langle \vec{T} \rangle$ , over an arbitrary closed, orientable surface  $S$  surrounding the object  $\mathbf{M}_{\text{opt}} = \oint_S (\mathbf{r} \times \langle \vec{T} \rangle \cdot d\mathbf{A})$ , where  $\mathbf{r}$  is the lever-arm vector from the particle center to the surface  $S$ . The components of the time-averaged MST were calculated as  $\langle T_{ij} \rangle = (1/2)\text{Re}[\epsilon_0 n^2 E_i E_j^* + \mu_0 H_i H_j^*] - (1/2)\delta_{ij}(\epsilon_0 n^2 |\mathbf{E}|^2 + \mu_0 |\mathbf{H}|^2)$ , where  $\mathbf{E}$  and  $\mathbf{H}$  are the total electric and magnetic fields, respectively, including incident as well as scattered contributions.  $n = 1.33$  is the refractive index of the surrounding medium. The absorption torque  $M_{\text{abs}}$  was calculated from the absorption cross section,<sup>30,35</sup> while the scattering torque is calculated to be  $M_{\text{sca}} = M_{\text{opt}} - M_{\text{abs}}$ . To calculate the power-dependent rotational dynamics, the laser intensity is approximated as  $I = P/\pi r_0^2$ , where  $P$  is the power of the 830 nm laser and  $r_0$  is an effective beam radius of the order  $r_0 \approx 600$  nm.



We used COMSOL Multiphysics 4.3 to perform finite element simulations to calculate the surface temperature of gold nanorods. In the COMSOL model, one gold nanorod is enclosed in a medium shell (diameter = 5  $\mu\text{m}$ ) with the thermal characteristics of water. The "Heat Transfer in Fluids" module was used, with the boundary temperature on the outside surface of the shell fixed at room temperature. The heat source was localized in the gold nanorod and was set to have a total power input of  $P_{\text{in}} = \sigma_{\text{abs}} P / \pi r_0^2$ , with the absorption cross section  $\sigma_{\text{abs}}$  provided by FDTD simulations. The initial temperature of the whole system was set at room temperature. We monitored the time-dependent temperature distributions and recorded the nanorod surface temperature after the system reached thermal equilibrium.

**Conflict of Interest:** The authors declare no competing financial interest.

**Acknowledgment.** This work was supported by the Knut and Alice Wallenberg Foundation. We thank Javier García de Abajo, Faegheh Hajizadeh, Halina Rubinsztein-Dunlop, Andreas Dahlin, Srdjan S. Acimović, and Tina Gschneidner for valuable comments and assistance.

**Supporting Information Available:** The Supporting Information is available free of charge on the ACS Publications website at DOI: 10.1021/acsnano.5b06311.

SEM images and extinction spectra of colloidal gold nanorods; scattering autocorrelation functions for a gold nanorod subject to circularly and linearly polarized laser; CMOS camera recorded snapshots and scattering signals showing rotation of a gold nanorod; polarized dark-field scattering spectra to verify the spinning orientation of gold nanorods; scattering spectra of gold nanorods measured in parallel by LCTF hyperspectral imaging; calculated optical force distribution for a gold nanorod illuminated by circularly polarized light; calculated surface temperature of a gold nanorod illuminated by laser; surface temperature of gold nanorods extracted from measured scattering autocorrelation signals; direct graphical comparison between experimentally measured and theoretically calculated rotational dynamic parameters of gold nanorods; laser power-dependent spinning frequency and temperature curves of the nanorods to examine their thermal stability; LSPR sensing data of gold nanorods; Table showing values of parameters for optical rotation calculation; procedure for growing gold nanorods; method for rod spinning frequency measurements; method for single nanoparticle dark-field scattering spectroscopy; procedures for spinning- and LSPR-based molecular sensing experiments. (PDF)

## REFERENCES AND NOTES

1. Feynman, R. P. There's Plenty of Room at the Bottom. *Caltech Eng. Sci.* **1960**, 23, 22–36.
2. Ozin, G. A.; Manners, I.; Fournier-Bidoz, S.; Arseneault, A. Dream Nanomachines. *Adv. Mater.* **2005**, 17, 3011–3018.
3. Ebbens, S. J.; Howse, J. R. In Pursuit of Propulsion at the Nanoscale. *Soft Matter* **2010**, 6, 726–738.
4. Judy, J. W. Microelectromechanical Systems (MEMS): Fabrication, Design and Applications. *Smart Mater. Struct.* **2001**, 10, 1115–1134.
5. Requicha, A. A. G. Nanorobots, NEMS, and Nanoassembly. *Proc. IEEE* **2003**, 91, 1922–1933.
6. Hasman, E. Plasmonics: New Twist on Nanoscale Motors. *Nat. Nanotechnol.* **2010**, 5, 563–564.
7. Chang, S. T.; Paunov, V. N.; Petsev, D. N.; Velev, O. D. Remotely Powered Self-Propelling Particles and Micropumps Based on Miniature Diodes. *Nat. Mater.* **2007**, 6, 235–240.
8. Rikken, R. S. M.; Nolte, R. J. M.; Maan, J. C.; van Hest, J. C. M.; Wilson, D. A.; Christianen, P. C. M. Manipulation of Micro- and Nanostructure Motion with Magnetic Fields. *Soft Matter* **2014**, 10, 1295–1308.
9. Fennimore, A. M.; Yuzvinsky, T. D.; Han, W.-Q.; Fuhrer, M. S.; Cumings, J.; Zettl, A. Rotational Actuators Based on Carbon Nanotubes. *Nature* **2003**, 424, 408–410.
10. Kim, K.; Xu, X. B.; Guo, J. H.; Fan, D. L. Ultrahigh-Speed Rotating Nanoelectromechanical System Devices Assembled from Nanoscale Building Blocks. *Nat. Commun.* **2014**, 5, 3632.
11. Wang, W.; Li, S. X.; Mair, L.; Ahmed, S.; Huang, T. J.; Mallouk, T. E. Acoustic Propulsion of Nanorod Motors Inside Living Cells. *Angew. Chem., Int. Ed.* **2014**, 53, 3201–3204.
12. Balk, A. L.; Mair, L. O.; Mathai, P. P.; Patrone, P. N.; Wang, W.; Ahmed, S.; Mallouk, T. E.; Liddle, J. A.; Stavis, S. M. Kilohertz Rotation of Nanorods Propelled by Ultrasound, Traced by Microvortex Advection of Nanoparticles. *ACS Nano* **2014**, 8, 8300–8309.
13. van den Heuvel, M. G. L.; Dekker, C. Motor Proteins at Work for Nanotechnology. *Science* **2007**, 317, 333–336.
14. Liu, M.; Zentgraf, T.; Liu, Y. M.; Bartal, G.; Zhang, X. Light-Driven Nanoscale Plasmonic Motors. *Nat. Nanotechnol.* **2010**, 5, 570–573.
15. Wang, J. Can Man-Made Nanomachines Compete with Nature Biomotors? *ACS Nano* **2009**, 3, 4–9.
16. Friese, M. E. J.; Nieminen, T. A.; Heckenberg, N. R.; Rubinsztein-Dunlop, H. Optical Alignment and Spinning of Laser-Trapped Microscopic Particles. *Nature* **1998**, 394, 348–350.
17. Arita, Y.; Mazilu, M.; Dholakia, K. Laser-Induced Rotation and Cooling of a Trapped Microgyroscope in Vacuum. *Nat. Commun.* **2013**, 4, 2374.
18. Maragò, O. M.; Jones, P. H.; Gucciardi, P. G.; Volpe, G.; Ferrari, A. C. Optical Trapping and Manipulation of Nanostructures. *Nat. Nanotechnol.* **2013**, 8, 807–819.
19. Lehmuskero, A.; Johansson, P.; Rubinsztein-Dunlop, H.; Tong, L. M.; Käll, M. Laser Trapping of Colloidal Metal Nanoparticles. *ACS Nano* **2015**, 9, 3453–3469.
20. Pelton, M.; Liu, M. Z.; Kim, H. Y.; Smith, G.; Guyot-Sionnest, P.; Scherer, N. F. Optical Trapping and Alignment of Single Gold Nanorods by Using Plasmon Resonances. *Opt. Lett.* **2006**, 31, 2075–2077.
21. Selhuber-Unkel, C.; Zins, I.; Schubert, O.; Sönnichsen, C.; Oddershede, L. B. Quantitative Optical Trapping of Single Gold Nanorods. *Nano Lett.* **2008**, 8, 2998–3003.
22. Yan, Z. J.; Pelton, M.; Vigdeman, L.; Zubarev, E. R.; Scherer, N. F. Why Single-Beam Optical Tweezers Trap Gold Nanowires in Three Dimensions. *ACS Nano* **2013**, 7, 8794–8800.
23. Lee, Y. E.; Fung, K. H.; Jin, D. F.; Fang, N. X. Optical Torque from Enhanced Scattering by Multipolar Plasmonic Resonance. *Nanophotonics* **2014**, 3, 343–350.
24. Ruijgrok, P. V.; Verhart, N. R.; Zijlstra, P.; Tchebotareva, A. L.; Orrit, M. Brownian Fluctuations and Heating of an Optically Aligned Gold Nanorod. *Phys. Rev. Lett.* **2011**, 107, 037401.
25. Zijlstra, P.; Paulo, P. M. R.; Orrit, M. Optical Detection of Single Non-Absorbing Molecules Using the Surface Plasmon Resonance of a Gold Nanorod. *Nat. Nanotechnol.* **2012**, 7, 379–382.
26. Li, J. F.; Huang, Y. F.; Ding, Y.; Yang, Z. L.; Li, S. B.; Zhou, X. S.; Fan, F. R.; Zhang, W.; Zhou, Z. Y.; Wu, D. Y.; et al. Shell-Isolated Nanoparticle-Enhanced Raman Spectroscopy. *Nature* **2010**, 464, 392–395.
27. Xu, H. X.; Bjerneld, E. J.; Käll, M.; Börjesson, L. Spectroscopy of Single Hemoglobin Molecules by Surface Enhanced Raman Scattering. *Phys. Rev. Lett.* **1999**, 83, 4357–4360.
28. Tong, L. M.; Miljković, V. D.; Käll, M. Alignment, Rotation, and Spinning of Single Plasmonic Nanoparticles and Nanowires Using Polarization Dependent Optical Forces. *Nano Lett.* **2010**, 10, 268–273.
29. Xu, X. H.; Cheng, C.; Xin, H. B.; Lei, H. X.; Li, B. J. Controllable Orientation of Single Silver Nanowire Using Two Fiber Probes. *Sci. Rep.* **2014**, 4, 3989.
30. Lehmuskero, A.; Ogier, R.; Gschneidner, T.; Johansson, P.; Käll, M. Ultrafast Spinning of Gold Nanoparticles in Water Using Circularly Polarized Light. *Nano Lett.* **2013**, 13, 3129–3134.
31. Ni, W. H.; Kou, X. S.; Yang, Z.; Wang, J. F. Tailoring Longitudinal Surface Plasmon Wavelengths, Scattering and Absorption Cross Sections of Gold Nanorods. *ACS Nano* **2008**, 2, 677–686.

32. Chen, H. J.; Shao, L.; Li, Q.; Wang, J. F. Gold Nanorods and Their Plasmonic Properties. *Chem. Soc. Rev.* **2013**, *42*, 2679–2724.
33. Ye, X. C.; Zheng, C.; Chen, J.; Gao, Y. Z.; Murray, C. B. Using Binary Surfactant Mixtures to Simultaneously Improve the Dimensional Tunability and Monodispersity in the Seeded Growth of Gold Nanorods. *Nano Lett.* **2013**, *13*, 765–771.
34. Chaumet, P. C.; Billaudeau, C. Coupled Dipole Method to Compute Optical Torque: Applications to a Micropropeller. *J. Appl. Phys.* **2007**, *101*, 023106.
35. Marston, P. L.; Crichton, J. H. Radiation Torque on a Sphere Caused by a Circularly-Polarized Electromagnetic Wave. *Phys. Rev. A: At., Mol., Opt. Phys.* **1984**, *30*, 2508–2516.
36. Kong, D. L.; Lin, W.; Pan, Y. X.; Zhang, K. K. Swimming Motion of Rod-Shaped Magnetotactic Bacteria: The Effects of Shape and Growing Magnetic Moment. *Front. Microbiol.* **2014**, *5*, 8.
37. Fogel'son, R. L.; Likhachev, E. R. Temperature Dependence of Viscosity. *Tech. Phys.* **2001**, *46*, 1056–1059.
38. Chandrasekhar, S. Stochastic Problems in Physics and Astronomy. *Rev. Mod. Phys.* **1943**, *15*, 1–89.
39. Risken, H. *The Fokker-Planck Equation*; Springer: Berlin, 1996.
40. Rings, D.; Schachoff, R.; Selmke, M.; Cichos, F.; Kroy, K. Hot Brownian Motion. *Phys. Rev. Lett.* **2010**, *105*, 090604.
41. Falasco, G.; Gnann, M. V.; Rings, D.; Kroy, K. Effective Temperatures of Hot Brownian Motion. *Phys. Rev. E* **2014**, *90*, 032131.
42. Hou, L.; Yorulmaz, M.; Verhart, N. R.; Orrit, M. Explosive Formation and Dynamics of Vapor Nanobubbles around a Continuously Heated Gold Nanosphere. *New J. Phys.* **2015**, *17*, 013050.
43. Hansen, P. M.; Bhatia, V. K.; Harrit, N.; Oddershede, L. Expanding the Optical Trapping Range of Gold Nanoparticles. *Nano Lett.* **2005**, *5*, 1937–1942.
44. Ma, H. Y.; Bendix, P. M.; Oddershede, L. B. Large-Scale Orientation Dependent Heating from a Single Irradiated Gold Nanorod. *Nano Lett.* **2012**, *12*, 3954–3960.
45. Bunea, A.-I.; Pavel, I.-A.; David, S.; Gáspár, S. Sensing Based on the Motion of Enzyme-Modified Nanorods. *Biosens. Bioelectron.* **2015**, *67*, 42–48.
46. Fang, J. J.; Zhu, T.; Sheng, J.; Jiang, Z. Y.; Ma, Y. Q. Thickness Dependent Effective Viscosity of a Polymer Solution near an Interface Probed by a Quartz Crystal Microbalance with Dissipation Method. *Sci. Rep.* **2015**, *5*, 8491.
47. Johnson, P. B.; Christy, R. W. Optical Constants of the Noble Metals. *Phys. Rev. B* **1972**, *6*, 4370–4379.
48. Emilsson, G.; Schoch, R. L.; Feuz, L.; Höök, F.; Lim, R. Y. H.; Dahlin, A. B. Strongly Stretched Protein Resistant Poly(ethylene glycol) Brushes Prepared by Grafting-To. *ACS Appl. Mater. Interfaces* **2015**, *7*, 7505–7515.